RSC Advances

PAPER

Cite this: *RSC Adv.*, 2020, **10**, 21158

Syngas production by bi-reforming methane on an Ni–K-promoted catalyst using hydrotalcites and filamentous carbon as a support material†

Adelino F. Cunha, *[ac] Sergio Morales-Torres, *[d] Luisa M. Pastrana-Martínez, [d] António A. Martins, [b] Teresa M. Mata, [b] Nídia S. Caetano [bc] and José M. Loureiro [a]

Steam reforming of methane (SRM) and dry reforming of methane (DRM) are frequently used in the production of syngas; however, the bi-reforming of methane (BRM) is an interesting and alternative process. In this study, BRM was studied over MgO, a layered double hydroxide (LDH) phase that was destroyed between 600 °C and 900 °C during the reaction. It showed good sorption capacity for CO_2 at relatively low temperatures (<500 °C), with CO_2 adsorption being a pre-requisite for its catalytic conversion. Among the tested materials, the potassium-promoted LDH showed the highest activity, achieving a maximum CO_2 conversion of 75%. The results suggest that at high temperature, the electronic structure of the used materials influences the destabilization of the feed in the order of methane, water and carbon dioxide. K promotes the catalytic activity, compensates the presence of large Ni particle sizes originating from the high metal loading, and favors the formation of Mg–Al-spinel. K is known to be an electronic promoter that releases electrons, which flow to the active metal. This electron flow induces instability on the molecule to be converted, and most probably, also induces size variations on the respective active nickel metal. The influence of the operating conditions in the range of 300 °C to 900 °C on the conversion of the reactants and product distribution was studied. Accordingly, it was concluded that it is only possible to obtain molar ratios of hydrogen-to-carbon monoxide close to two at high temperatures, a pre-requisite for the synthesis of methanol.

Received 11th April 2020
Accepted 14th May 2020

DOI: 10.1039/d0ra03264f

rsc.li/rsc-advances

1. Introduction

Since the dawn of the industrial revolution, starting in late 18th century,[1] the ever increasing demand for energy and chemicals to support the growing development of human society has been essentially provided through the utilization of non-renewable resources. This has resulted not only in significant environmental impacts, for example climate change,[2] but also economic burdens.

Accordingly, a possible solution for the abovementioned issues is the catalytic bi-reforming of methane (BRM), in which methane reacts with carbon dioxide and water to obtain syngas according to the chemical reaction (a): $\Delta_r G^\circ$ (Gibbs free enthalpy) = $\Delta_r H^\circ$ (reaction enthalpy) − T (reaction temperature) × $\Delta_r S^\circ$ (reaction entropy)

$$3CH_4 + 2H_2O + CO_2 \rightleftharpoons 4CO + 8H_2,\ \Delta_r G^\circ = (747.6\ \text{kJ mol}^{-1} - T\ (\text{K}) \times 780.2\ \text{J mol}^{-1}\ \text{K}^{-1}) \quad (a)$$

Catalytic BRM is a combination of steam reforming of methane SRM[3] (b) and dry reforming of methane DRM[4] (c):

$$CH_4 + H_2O \rightleftharpoons CO + 3H_2,\ \Delta_r G^\circ = (250.1\ \text{kJ mol}^{-1} - T\ (\text{K}) \times 189.7\ \text{J mol}^{-1}\ \text{K}^{-1}) \quad (b)$$

$$CH_4 + CO_2 \rightleftharpoons 2CO + 2H_2,\ \Delta_r G^\circ = (247.3\ \text{kJ mol}^{-1} - T\ (\text{K}) \times 400.8\ \text{J mol}^{-1}\ \text{K}^{-1}) \quad (c)$$

In most of the literature published, Ni is preferred as the active phase.[5]

Syngas production is an intermediate step for several synthetic processes.[6] Accordingly, the idea of using catalytic

[a]*Laboratory of Separation and Reaction Engineering, Associate Laboratory LSRE-LCM, Department of Chemical Engineering, Faculty of Engineering, University of Porto, Rua Dr. Roberto Frias, 4200-465, Porto, Portugal*

[b]*LEPABE – Laboratory for Process Engineering, Environment, Biotechnology and Energy, Faculty of Engineering, University of Porto, Rua Dr. Roberto Frias, 4200-465 Porto, Portugal*

[c]*School of Engineering (ISEP), Polytechnic of Porto (P.Porto), R. Dr. António Bernardino de Almeida 431, 4249-015 Porto, Portugal. E-mail: afccu@isep.ipp.pt; Fax: +351 22 83 21 159; Tel: +351 22 83 41 904*

[d]*Carbon Materials Research Group, Department of Inorganic Chemistry, Faculty of Sciences, University of Granada, Avenida de Fuentenueva, s/n, 18071, Granada, Spain. E-mail: semoto@ugr.es; Fax: +34 958248526; Tel: +34 958240443*

† Electronic supplementary information (ESI) available. See DOI: 10.1039/d0ra03264f

BRM has already been considered and theoretically discussed in previous reports;[7–10] however, there is a lack of experimental work. Thus, more experimental work is required in this area.[11–16]

The strongly endothermic BRM reaction requires an efficient catalyst. The material to be used as a support for the active phases and promoters must show thermal stability, which can be achieved for example by a porous metallic ribbon structure.[17] Another required feature is high thermal conductivity to ensure efficient heat transfer into the reaction zone.[18,19] Furthermore, basicity is required to reduce carbonization, which can be achieved using MgO.[20,21] In addition, inducing the dispersion of crystallites (in this work Ni) of the reduced active phase is desirable, whereas the formation of solid solutions with oxides of the active nickel phase is unfavorable.[22] Furthermore, a highly dispersed Ni active phase is not only desirable, but also crucial to allow the best combination of coking prevention and increase in active phase surface area. The presence of a solid solution after reduction treatments can be explained by the hindered reduction of the Ni^{2+} cations embedded in the lattice of the hardly reducible MgO.[13] A similar situation occurs for the structural characteristics of the catalytic material, which itself should act as a catalytically active phase or as a promoter towards the active phase. Further details to support the choice of Ni can be found in previously published related work.[9] Finally, the catalytic material to be applied in BRM should have the ability to adsorb sufficient CO_2 in the form of a metastable or intermediate complex to ensure its successful reaction with CH_4. Therefore, materials with the ability to adsorb CO_2 are suitable candidates, and among the existing possibilities, hydrotalcite-like materials are commonly used as commercial adsorbents/molecular sieves. In the case of hydrotalcite-like materials, selective and suitable CO_2 adsorption is also possible at temperatures as high as 400 °C.[23] LDHs are excellent support materials due to their ability to adsorb CO_2, and most importantly, their alkaline properties, which reduce the formation of coke deposition.

Potassium is frequently used in reforming catalysts. It reduces/avoids the formation of coke,[24] can enhance the sorption capacity of carbon dioxide,[25] and acts as electronic promoter/activator.[26] Moreover, potassium oxide promotes the adsorption of water,[27] which increases the gasification of carbon. However, the higher the reaction temperature, the lower the adsorption or sticking of the molecules on the catalyst surface because adsorption is an exergonic process favoured at lower temperatures. Finally, a potassium-promoted LDH can act as an active catalytic phase in the WGSR.[28]

The objective of this work was to develop an Ni catalyst supported on an LDH with K as a promoter for catalytic BRM, and to compare its performance with other comparable catalysts reported in the literature. The main focus was the modifications performed to obtain a material that can catalyze BRM at lower temperatures and to obtain a hydrogen-to-carbon monoxide ratio close to two in the obtained syngas, a prerequisite for the production of methanol.

2. Experimental

2.1 Catalyst synthesis

Fig. 1 depicts the chemical structure of an LDH/hydrotalcite-like compound (HTlc) similar to that used in this work. The LDH or HTlc are ionic materials composed of layers of hydroxide anions combined with layers of metal cations, anions or neutral molecules, in which the ions are weakly bound and maybe interchanged easily.

Pellets of commercial HTlc or LDH, simple or doped with potassium-oxide, PURAL MG30 (aluminum magnesium hydroxide, with 70 mol% Al_2O_3) from Sasol, were used for the catalytic BRM tests, or as a support material for other catalytically active phases. The synthesis and characterization procedure for the materials used was described in detail in a previous report.[29] This type of material was chosen as the catalyst support because it is known to be a good carbon dioxide sorbent at moderate temperatures (200–450 °C) and is used for many catalytic reactions.[25,30]

The materials used in this work were named according to the support material, *i.e.*, depending on if it is a commercial hydrotalcite-like compound, and the percentages of each phase/compound loaded. The acronym LDH stands for layered double hydroxide. For example, $LDHK_2O^{20}Ni^{17}$ corresponds to K_2O and Ni loadings of 20% and 17%, respectively, and $LDHK_2O^{20}$ corresponds to a potassium oxide loading of 20.0 wt% supported on LDH. The LDH and LDH doped with potassium were both commercial products.

To produce the catalysts, the required amount of phases selected, such as $Ni(NO_3)_2 \cdot 6H_2O$, were weighed and dissolved in 200 mL of water. Subsequently, the pellets of the support material were added to this solution, and the mixture was treated under ultrasonication at 100 °C for 2 h. The suspension was dried at 110 °C for 48 h. All the materials available were loaded into the catalytic reactor. Then, they were calcined for 48 h at 600 °C under a nitrogen flow of 5 N cm^3 min^{-1}. Finally, the catalyst samples were activated in pure hydrogen (10 N cm^3 min^{-1}) at 700 °C for 24 h. Before the start of the BRM reaction, the material with Ni as the active phase, $LDHK_2O^{20}Ni^{17}$, was subject to a treatment with a gas stream of carbon monoxide at a flowrate of 25 N cm^3 min^{-1} at 400 °C for 2 h. This

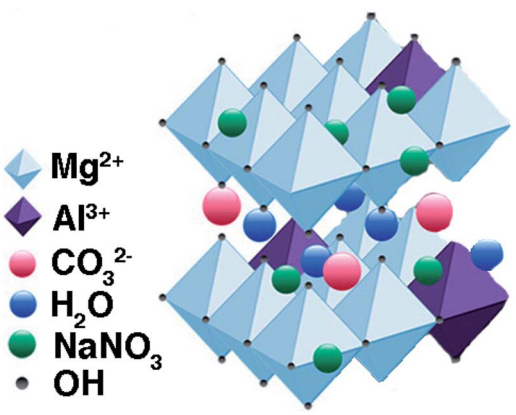

Fig. 1 Chemical structure of LDH, adapted from ref. 31 and 32.

was done because during the Boudouard reaction (BD), as represented in eqn (d), carbon monoxide decomposes into carbon dioxide and carbon.

After the synthesis of the $LDHK_2O^{20}Ni^{17}$ material, the amount of carbon monoxide converted during BD treatment under steady-state conditions for a period 2 h was 50%, and thus the total amount of carbon formed was 6 mg. The amount of carbon produced was calculated by monitoring the Boudouard reaction on a gas chromatograph. In addition, before starting BRM, the material used was gravimetrically analyzed. In addition, and for clarification, the hydrogen pre-treated material in this work was designated as $LDHK_2O^{20}Ni^{17}$, while the material pre-treated with BD reaction and after BRM was denoted as $LDHK_2O^{20}Ni^{17}$-u (u stands for used). It must be stressed that neither the LDH nor $LDHK_2O^{20}$ material has been subject of pre-treatment using the BD reaction.

$$2CO \rightarrow C + CO_2,\ \Delta_r G^\circ = (172.4\ \text{kJ mol}^{-1} - T\ (\text{K}) \times 320.2\ \text{J mol}^{-1}\ \text{K}^{-1}) \quad \text{(d)}$$

In an ideal scenario, the carbon produced is just a metal-filamentous composite material consisting of carbon fibers with Ni particles on their tips.[33,34] In the context of catalytic hydrogenation/dehydrogenation reactions, it has been reported that the best catalytic results were obtained by the preparation of nickel nanoparticles, showing better activity, selectivity and stability than conventional Ni catalysts due to the filamentous carbon support materials, which stabilized the nanoparticles, preventing surface migration and coalescence during reactions at high temperatures. Furthermore, they may also influence the course of the reaction. The purpose of a Boudouard reaction pre-treatment within a short period is to detach small Ni crystallites from the bulk phase of the metal so that reaction activity is enhanced. The reason why a short period used was to minimize the eventual leaching of the Ni phase due to the possible formation of an intermediate nickel-tetracarbonyl *via* the Mond process. Finally, the Ni nanocatalysts exhibited excellent stability under air, with no special care required for their storage. This is the reason why in this study the aim was to generate Ni nanoparticles on carbon filaments by decomposing carbon monoxide in a disproportionation reaction releasing carbon dioxide, and especially forming carbon filaments as a composite material *via* the disintegration of Ni particles from the top of the original $LDHK_2O^{20}Ni^{17}$ material.[34,35]

2.2 Catalyst characterization

The materials were characterized before and after the BRM runs, applying different physical–chemical techniques. The detailed equipment specification can be found elsewhere.[33]

The elemental compositions of the materials were determined *via* inductively coupled plasma atomic emission spectroscopy (ICP-AES) analysis, and the chemical composition of the starting materials was determined *via* X-ray fluorescence spectroscopy and X-ray photoelectron spectroscopy (XPS). XPS spectra were obtained using a Kratos Axis Ultra-DLD X-ray photoelectron spectrometer equipped with an MgK_α X-ray source ($h\nu$ = 1253.6 eV) operating at 12 kV and 10 mA, and a hemispherical electron analyzer. Survey and multi-region spectra were recorded at the O1s and Ni2p photoelectron peaks. X-ray powder diffraction (XRD) patterns were recorded within the range of 10–80° (2θ) with a Bruker D8 Advance diffractometer equipped with a CuK_α radiation source at a wavelength (λ) of 1.541 Å. JCPDS files were searched to assign the different observed diffraction lines, and the average crystal size was determined using the Scherrer equation.

The morphology of the materials was examined by scanning electron microscopy (SEM) using an AURIGA (FIB-FESEM) microscope from Carl Zeiss SMT equipped with an EDAX microanalysis system. TEM was carried out using an FEI Titan G2 60-300 microscope with a high brightness electron gun (X-FEG) operated at 300 kV and equipped with a Cs image corrector (CEOS). For analytical electron microscopy (AEM), a SUPER-X silicon-drift windowless EDX detector was used. High-angle annular dark-field scanning TEM (HAADF-STEM) images were taken at almost just focus. Textural characterization of the fresh materials was carried out by physical adsorption of N_2 at −196 °C using a Quantachrome Autosorb-1 instrument. The apparent surface area of the catalyst and supporting material, S_{BET}, was determined by applying the BET equation,[36] while the BJH method[37] was applied the desorption branch of the N_2 isotherms to obtain the average pore diameter (d_{pore}).

2.3 Reaction studies

The commercial materials used for catalytic BRM, LDH and $LDHK_2O^{20}$ were kept in their original bead shapes (pellets). The Ni-impregnated materials were tested as a fine powder. It was assumed that the crystal structures of the respective compounds present in the fine powder were maintained; however, it is possible that the crystal structure was deformed along the c-axis during mechanical treatment or bonds were displaced irreversibly (bond rupture). The smaller particles together with rough surfaces contribute to a better interaction during reaction.

The reaction studies were carried out in a 42 cm-long tubular stainless steel fixed-bed continuous down-flow reactor with an inner diameter of 3.3 cm, corresponding to a volume of 350 cm^3. Details about the reactor setup can be found in previous studies.[10] Catalytic experiments were performed at temperatures between 600 °C and 900 °C, with a $CH_4 : H_2O : CO_2$ molar feed ratio of 3 : 2 : 1. During the startup procedure, the temperature was increased by increments at a heating rate of 5 °C min^{-1} of the pure inert gas stream, either helium or nitrogen, depending on the experiment, until reaching the desired reaction temperature. The temperature inside the reactor (center of the reaction zone) was monitored with a thermocouple. For all the measurements, an average reproducibility error of ±5% was considered.

Before the experimental runs, a blank experiment without the presence of any catalyst was carried out to ensure the absence of reactor activity due to its stainless steel material nature. For the blank experiment, quartz wool was used and the temperature was increased from 400 °C to 900 °C in increments of 50 °C. The flowrates and molar feed ratios were the same as that used in the experimental runs, and samples were taken at

each temperature. No catalytic activity was measured, and thus subtraction of the blank experiment results at the corresponding conditions was not necessary.

The catalyst, which was produced as described in Section 2.1, was reloaded into the reactor and thermally treated for 48 h at 600 °C under an N_2 flow of 5 N cm^3 min^{-1}. During the catalytic BRM tests, each temperature increment was evaluated for at least 6 h time-on-stream to ensure stable operating conditions. The effects of temperature and flowrate (contact time) were then studied. The inlet molar flowrate of the reactant methane $\dot{n}_{CH_4,0}$ = 1.233 mmol min^{-1} ($\dot{V}_{inert,0}$ = 30 N cm^3 min^{-1}), unless otherwise stated. Thus, the total molar flow rate of the reactants for a steam-to-carbon ratio (R) of 0.5 was 2.466 mmol min^{-1} (corresponding to 3 × 0.411 mmol min^{-1} of methane plus 2 × 0.411 mmol min^{-1} of water plus 1 × 0.411 mmol min^{-1} of carbon dioxide). This reactant flowrate was kept constant, while different inert gas flow rates were used (from 0 to 50 N cm^3 min^{-1}). For example, when the inert gas-to-carbon ratio (I) equaled 1.25, an inert gas flow rate of 50 N cm^3 min^{-1} (inert gas molar flowrate of 2.055 mmol min^{-1}) was mixed with 1.644 mmol min^{-1} of CH_4 (3 × 0.411 mmol min^{-1}) plus CO_2 (0.411 mmol min^{-1}) in the feed.

The water conversion was estimated from the measured amounts of hydrogen formed in the reaction (indirect method). According to the SRM equation (eqn (c)) present in the overall BRM equation, for 6 mol of hydrogen formed, 2 mol of water is consumed. Therefore, during the conducted BRM experiments, the compounds exiting the reactor were first passed through a large water trap, then through a condenser (stainless steel heat exchanger consisting of a bundle of tubes), and finally through an ice-cooled Dewar trap. The unreacted liquid water was periodically collected in the two traps and analyzed to determine the amount of water produced. In most of the cases, the estimated amount of water did not deviate by more than ±5% from the water collected in the traps.

The conversion of the reactants (CH_4, CO_2 and H_2O) was calculated as follows:

$$X_{CH_4}[\%] = \frac{\dot{n}_{CH_4,0} - \dot{n}_{CH_4}}{\dot{n}_{CH_4,0}} \times 100\% \quad (1)$$

$$X_{CO_2}[\%] = \frac{\dot{n}_{CO_2,0} - \dot{n}_{CO_2}}{\dot{n}_{CO_2,0}} \times 100\% \quad (2)$$

$$X_{H_2O}[\%] = \frac{\dot{n}_{H_2O,0} - \dot{n}_{H_2O}}{\dot{n}_{H_2O,0}} \times 100 \quad (3)$$

where $\dot{n}_{CH_4,0}$, $\dot{n}_{CO_2,0}$ and $\dot{n}_{H_2O,0}$ represent the molar flowrates of CH_4, CO_2 and H_2O in the feed and $\dot{n}_{CH_4}$, $\dot{n}_{CO_2}$ and $\dot{n}_{H_2O}$ are the outlet molar flowrates of the reactants, respectively. The molar fraction y_i (or partial pressure) was calculated for all species present in the outlet gas stream using eqn (4):

$$y_i = \frac{\dot{n}_i}{\sum_i^n \dot{n}_i} = \frac{p_i}{p_{total}}; \quad p_{total} = \sum_i^n p_i \quad (4)$$

where $\dot{n}_i$ represents the molar flowrate of species i and $\sum_i^n \dot{n}_i$ represents the total molar flowrate of all the species in the outlet stream. The equilibrium conversions and reactant/product composition are shown graphically below in the Results and discussion section.

The yield of species i was calculated using eqn (5):

$$Y_i(\%) = \frac{\bar{n}_i - \dot{n}_{i,0}}{\dot{n}_{CO_2,0}} \frac{\nu_{CO_2}}{\nu_i} \times 100\% = \frac{\dot{n}_{CO}}{4 \times \dot{n}_{CO_2,0}} \times 100\% \text{ or } \frac{\dot{n}_{H_2}}{8 \times \dot{n}_{CO_2,0}} \times 100\% \quad (5)$$

with $\dot{n}_{i,0} = 0$ due to the absence of both H_2 and CO in the inlet. The stoichiometric coefficient ν_i is defined as $\nu_{CH_4} = 3$, $\nu_{CO_2} = 1$, $\nu_{H_2O} = 2$, $\nu_{H_2} = 8$, $\nu_{CO} = 4$ according to the BRM chemical reactions (Reactions (a)–(c)). The selectivity of species i can be obtained using eqn (6):

$$S_i = \frac{Y_i}{X_{CO_2}} = \frac{Y_{CO}}{X_{CO_2}} \text{ or } \frac{Y_{H_2}}{X_{CO_2}} \quad (6)$$

Considering a carbon dioxide inlet flow of 0.411 mmol min^{-1} for full conversion, in agreement with the stoichiometry of the reaction, the maximum hydrogen yield possible for BRM is $Y_{i,max}$ = 3.288 mmol min^{-1} H_2/(8 × 0.411 mmol min^{-1} CO_2), which corresponds to the maximum possible selectivity of $S_{i,max}$ = 1.

Finally, the materials used in this work were weighed after the experimental runs to investigate the possible formation of coke.

3. Results and discussion

3.1 Characterization of materials

The properties of the base materials, including LDH[38] and $LDHK_2O$[20],[25,29,39] used as catalysts for BRM were determined in previous works and used in this work as needed.

Table 1 summarizes the relevant physical–chemical properties of the materials before and after the BRM experiments, in particular metal composition (obtained from ICP-AES), BET surface area and average pore diameter (obtained from N_2 adsorption/desorption isotherms), as well as promoter and Ni content (obtained from EDX). The values with an associated reference were determined in previous works.

3.1.1 Nitrogen physisorption. The LDH support showed a relatively high BET surface area. However, upon the addition of promoters (*e.g.*, K_2O in $LDHK_2O$[20]) and Ni as the active phase (*e.g.*, Ni in $LDHK_2O$[20]Ni[17]), treatments such as calcination and reduction with hydrogen, and BRM reaction (*e.g.* $LDHK_2O$[20]Ni[17]-u), an important reduction in the surface area of the materials was observed due to pore blockage and sintering.

The adsorption isotherm for $LDHK_2O$[20]Ni[17] before BRM can be classified as type II (Fig. S1, ESI†), associated with a hysteresis loop of type H4. According to IUPAC, the reversible type II isotherm corresponds to non-porous or macroporous adsorbing materials, corresponding to light unrestricted monolayer-

Table 1 Composition and physical–chemical properties of the materials used[a]

Catalyst	m_{cat} (g)	$X:Y:Z$, $K_2O/MgO/Al_2O_3$ (mass%)	Ni content (wt%)	S_{BET} ($m^2\ g^{-1}$)	d_{pore} (nm)
LDH	40	0 : 29 : 71	—	200	8
$LDHK_2O^{20}$	40	20 : 23 : 57	—	62	17
$LDHK_2O^{20}Ni^{17}$	15	17 : 19 : 48	16.7	39	9
$LDHK_2O^{20}Ni^{17}$-u	15	17 : 19 : 48	16.7	28	12

[a] m_{cat}: weight of catalyst used during the experimental run.

multilayer adsorption. It was also observed that the inflection point, where the beginning of almost the linear middle section of the isotherm occurs, appeared very early, meaning that the monolayer coverage was quickly completed, and multilayer adsorption was dominant. It can be also observed that hysteresis loops are present. They can be interpreted as being between type H3 and type H4, *i.e.* aggregates of plate-like particles are expected to exist in the analyzed materials with a significant presence of slit-shaped pores or narrow slit-like pores.

The isotherm for the catalyst after BRM was similar to that obtained before performing the experiment, although slightly lower volumes of adsorbed N_2 were observed at low and high relative pressures (Fig. S1†), indicating the slight blockage of the micropores and narrow mesopores, respectively. The Ni-supported catalysts (before BRM) showed lower BET surface areas than their corresponding support (Table 1), in particular 200 and 39 $m^2\ g^{-1}$ for LDH and $LDHK_2O^{20}Ni^{17}$, respectively. This decrease in surface area is a result of the decrease in porosity, where this can be explained by the blockage of the micropores induced by the metal particles, which became larger after the sintering occurring during the calcination and reduction treatments. This fact is easier to observe in the samples used in the BRM reaction, in which the decrease in the BET surface area is larger due to even stronger particle sintering (*e.g.*, 28 $m^2\ g^{-1}$ for $LDHK_2O^{20}Ni^{17}$-u). Thus, it is expected that the micropores are progressively blocked, and the larger pores become dominant in the surface of the catalysts after BRM. Specifically, the pore diameter of the spent catalyst increased from 9 nm to 12 nm for $LDHK_2O^{20}Ni^{17}$-u.

3.1.2 X-ray diffraction (XRD). XRD is the preferred technique to characterize the bulk structure of materials (phase composition, structural properties, and crystal size). The phase composition may help in the evaluation of the sorption and activation of carbon dioxide characteristics of the various materials, as well as the sorption and activation of the methane and water molecules involved. The XRD patterns of the materials synthesized before and after the BRM tests can be found in Fig. 2 and Table S1† lists the bulk phases with the corresponding 2θ positions, with "-u" corresponding to the patterns for the catalyst used in the BRM reaction.

Concerning the XRD patterns of the LDH, the results agree well with previous reports,[38] and they clearly depict a hydrotalcite-like structure. Moreover, it was found that the LDH structure was destroyed at 600 °C, in agreement with earlier studies.[40–42] It was also reported that at a temperature higher than 600 °C, the destruction of the LDH structure is accompanied by the formation of periclase MgO, which is similar to pure MgO.[43] Weak, broad peaks for $MgAl_2O_4$ (35°, PDF no. 21-1152) and γ-Al_2O_3 (66°) were also observed in the patterns of LDH (Table S1†), and a spinel phase was formed at a higher intensity after calcination of LDH at 700 °C. The peaks of the periclase structure in LDH are broad and low in intensity. The potassium-promoted hydrotalcite material (*i.e.*, $LDHK_2O^{20}$ before the test) was also analyzed in a previous study and its XRD patterns correspond to a typical LDH structure, matching the patterns reported for aluminum magnesium hydroxy carbonate ($Mg_2Al_2(OH)_8CO_3 \cdot xH_2O$, Table S1†).

The Ni-supported catalysts with the same metal loadings reduced before BRM (Fig. 2) showed the presence of metallic nickel (Ni), nickel(II)-oxide (NiO), K_2O, and an HTlc structure, as expected. The NiO phase became dominant due to the high metal loading of the samples (16.7 wt%). Since the samples were activated before BRM, and XRD only reflects the structure of the bulk phase rather than the surface structure, it was expected that the NiO phase most probably appears in abundance in the bulk structure due to the very high loadings of the catalyst prepared, where NiO in the bulk phase would not have been reduced. Similar behavior was previously found[44] on an Ni-based catalyst with high metal loadings. However,

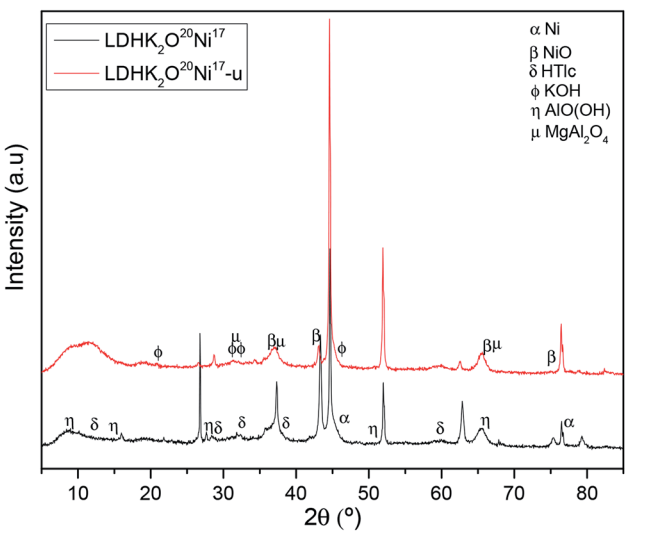

Fig. 2 XRD patterns of the catalysts before and after the BRM tests. Colors and symbols are used for better visibility and identification.

Table 2 Ni crystal sizes obtained using the Scherrer equation and the XRD data

Material	Treatment	d_{Ni} (nm)	Reference
$LDHK_2O^{20}Ni^{17}$	H_2 reduced	42.1	This work
$LDHK_2O^{20}Ni^{17}$-u	After BRM	41.0	
$NiAl_2O_3$	H_2 reduced	3.3	10
	After BRM	7.6	
$NiAl_2O_3$[a]	H_2 reduced	5.4	15
	After BRM	8.2	
NiMgO[b]	H_2 reduced	10	13
$NiZrO_2$[c]	H_2 reduced	13.4	12

[a] *In situ* H_2 reduced at 800 °C for 3 h, and spent at 800 °C for 40 h with a GHSV of 138 L $(g_{cat}\ h)^{-1}$. [b] *In situ* H_2 reduced at 900 °C. [c] *In situ* H_2 reduced at 650 °C for 2 h.[47].

$LDHK_2O^{20}Ni^{17}$-u showed almost the presence of metallic and only residual amounts of NiO, while $LDHK_2O^{20}Ni^{17}$ showed both Ni and NiO phases in the bulk. The obvious explanation for this is the pre-treatment used with CO (BD-reaction) probably significantly reduced the NiO in the bulk. As also observed in Table 3, the crystal size of $LDHK_2O^{20}Ni^{17}$-u is slightly lower than that for $LDHK_2O^{20}Ni^{17}$, which is further confirmation.

After the severe temperature conditions of the BRM reaction at 800 °C (*i.e.*, $LDHK_2O^{20}Ni^{17}$-u), part of the LDH structure was destroyed to form magnesium aluminum oxide ($MgAl_2O_4$). The appearance of $MgAl_2O_4$ (probably a spinel-structure) indicates that there is a strong interaction between MgO and AlO(OH)/Al_2O_3, which may also influence the active Ni phase in the BRM process.

Additionally, carbon deposition was detected in the XRD pattern since both Ni catalysts were pre-treated under Boudouard reaction conditions. However, during the BRM reaction, carbon deposition is not expected to occur. According to previous studies,[45,46] carbon deposition can be suppressed using high water-to-carbon ratios or by the presence of carbon dioxide.

Small crystal sizes of the active Ni phase are essential to obtain good catalytic activities. Table 2 presents the Ni crystal sizes of the catalytic materials prepared, which were obtained from the diffraction patterns using the Debye–Scherrer equation. The crystallite size of Ni in the synthesized catalytic materials was determined to be around 40 nm (Table 3). Additionally, the crystal sizes of some materials reported in the literature were introduced for comparison.

Table 3 Chemical composition of the catalysts before and after the BRM determined by XPS analysis

	Atomic content (at%)					
Material	O	C	Ni	Al	K	Mg
$LDHK_2O^{20}Ni^{17}$	65.0	10.5	6.0	12.5	2.5	3.5
$LDHK_2O^{20}Ni^{17}$-u	61.3	18.3	3.9	11.4	2.0	3.1

$$\tau = \frac{K\lambda}{\beta \cos\theta}$$

τ: mean size of the crystalline, which may be smaller or equal to the grain size, which may be smaller or equal to the particle size. K: dimensionless shape factor, with a value close to unity. The shape factor has a typical value of about 0.9 (spherical shape). λ: X-ray wavelength. β: line broadening at half the maximum intensity (FWHM) after subtracting the instrumental line broadening, in radians. θ: Bragg's angle.

Considering the method of impregnation used and the diameters of the cavities and pores of the LDH, it is not expected that all the Ni will be inside the pores. The most obvious occurrence, and considering that K_2O is also present, is that some of the Ni will be segregated to the periphery of the LDH or aggregated with K_2O and/or the LDH. Thus, even after hydrogen reduction, the dispersion of Ni is hindered, which explains the bigger crystal size of Ni in $LDHK_2O^{20}Ni^{17}$ in comparison to that of $LDHK_2O^{20}Ni^{17}$-u after BRM. Since the reaction was conducted at temperatures above that for the thermal decomposition of LDH, it is clear that the dispersion of Ni is low and insignificant, which explains the relatively high crystal sizes obtained. Finally, Ni-based catalysts used for steam reforming of ethanol have demonstrated that the higher the metal loading, the larger the final crystal size, especially after the reaction.[48] Consequently, the higher the metal loading, the more dominant the NiO phase becomes, and since the materials were activated before the BRM, their XRD patterns reflect the structure of their bulk phase rather than their surface, and NiO in the bulk phase was not reduced.[44] Therefore, the NiO present in the bulk phase may interact with the reduced Ni on the surface, also probably influencing the crystal size.[46]

Here, it must also be stressed that $LDHK_2O^{20}Ni^{17}$-u shows a crystal size of 41.0 nm and this value is in excellent agreement with another material that was prepared by CVD.[33,34] Most likely, the pre-treatment performed using the BD reaction resulted in the formation of small Ni crystals, which significantly reduced the tendency of sintering. Nevertheless, no filaments were detected with Ni on top (evidence in SEM and TEM images in Sections 3.1.3 and 3.1.4, respectively). This fact may be due to the loading of Ni used in this work, which was only 17 wt%. In general, a high metal loading or massive catalyst is required for the mentioned purpose.[49]

3.1.3 Scanning electron microscopy (SEM). The morphology of the synthesized materials was studied by scanning electron microscopy (SEM), as depicted in Fig. 3. Before the catalytic BRM, LDH showed a typical platelet-like morphology. However, under the severe temperature conditions used ($T_{reaction}$ = 400–900 °C), the morphology of LDH changed. The same phenomenon was also observed for the $LDHK_2O^{20}$ material. In addition, the EDX and ICP-AES analyses showed that LDH has a ~29% magnesium oxide content. This Mg content is consistent with the expected nominal values of the Mg and Al content (Table 1).

The $LDHK_2O^{20}Ni^{17}$ catalyst exhibited two types of morphologies, which were more evident on the surface of the extrudates (Fig. 3a–c). The external surface exhibit "agglomerates" of up to

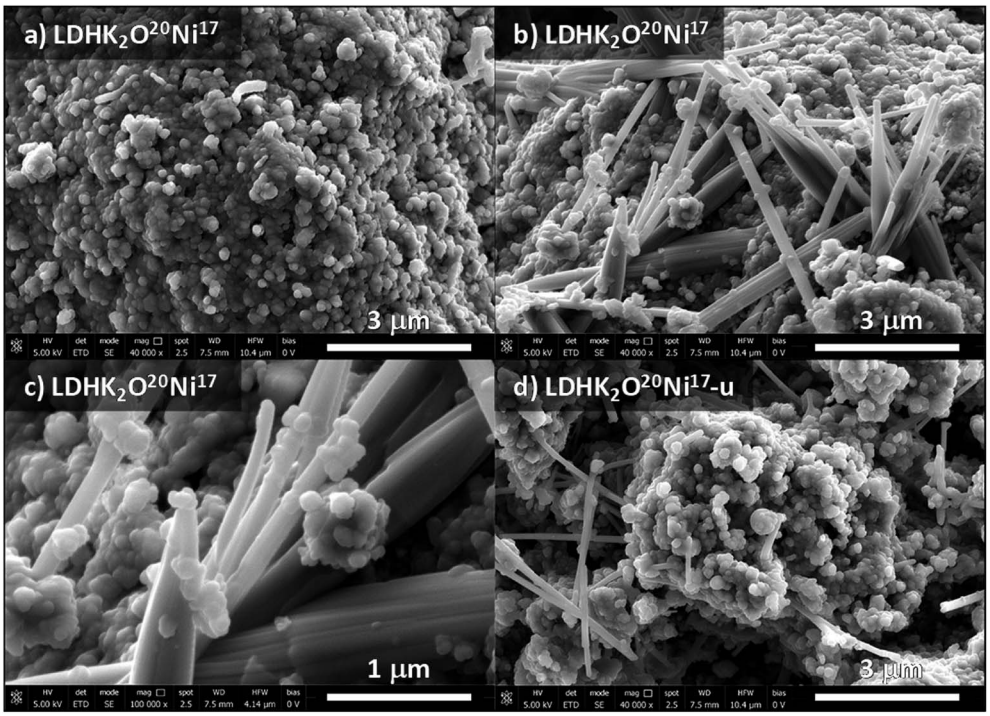

Fig. 3 SEM images of the catalysts. Different coexisting morphologies of $LDHK_2O^{20}Ni^{17}$ (a–c) before and (d) after the BRM reaction.

500 nm in diameter (Fig. 3a), coexisting "needle-like" structures (Fig. 3b and c) up to 5 μm in length. Together with the EDX spectra (not shown), it was found that the amount of potassium in the "needle-like" structures was higher than that detected in the agglomerates. These "needle-like" structures have been reported earlier (Fig. S2, ESI†). The "needle-like" morphology was also present in the inner part of the extrudates, although their amount and size were much smaller. The used catalyst after performing the BRM reaction also showed a mixture of thin "needle-like" particles (Fig. 3d), together with large clusters of agglomerates, with larger pores, in agreement with the N_2 adsorption isotherms (Fig. S1†).

3.1.4 Transmission electron microscopy (TEM). The metal distribution on the different supports and the particle size were analyzed by transmission electron microscopy, and the results are shown in Fig. 4. As already evidenced by SEM observations, two types of structures can be identified on the $LDHK_2O^{20}Ni^{17}$ sample (Fig. 4a and b), "needle-like" and "agglomerates", which the latter being more abundant. In fact, the Ni distribution on the "agglomerates" seems to be better than on the "needle-like" structure. In general, a homogenous metal distribution throughout the $LDHK_2O^{20}Ni^{17}$ material was achieved (Fig. 4b).

Upon analyzing the material after the BRM, clear particle sintering was observed (Fig. 4c and d), in particular for $LDHK_2O^{20}Ni^{17}$-u, in which large spherical nickel particles were observed on the material surface after the reaction (*i.e.*, Fig. 4b *vs.* Fig. 4d).

3.1.5 X-ray photoelectron spectroscopy (XPS). The surface chemistry of the catalysts before and after BRM was characterized by XPS (Fig. S5†), showing the deconvoluted O1s and Ni2p regions of the fresh and spent catalysts, while their atomic composition (at%) is listed in Table 4.

The O1s spectra of the samples could be deconvoluted into two components located at ~530.4 and ~533.2 eV (Fig. S5a†). The first peak can be assigned to the surface lattice oxygen (O^{2-}) of Al_2O_3, K_2O or MgO, whereas the other peak at a high binding energy (BE) corresponds to hydroxides (OH^-).[50] In general, all the catalysts presented a higher intensity for the second peak regardless of being fresh or used.

The XPS Ni2p spectra of the catalysts is shown in Fig. S5b.† The spectra clearly reveal the presence of surface nickel in both the metallic and oxidized states for the fresh and spent materials. The very small $2p^{3/2}$ photoelectron peak observed at ~853 eV corresponds to metallic nickel. For all the samples, a strong peak located at ~856 eV was observed, which is designated as Ni $2p_{3/2}$ and attributed to Ni^{2+} from NiO, in agreement with the XRD results.[50] A typical doublet (separated by 18.0 eV) can also be observed. Besides, shake-up (satellite) peaks can also be seen in the region at about 6.0 eV higher than the normal $2p^{3/2}$ and $2p^{1/2}$ bands. The other peaks located at higher BE are attributed to Ni $2p_{1/2}$ and its satellite.[51] The intensity of the main peak and the BE is similar between the two samples, and thereby, the Ni^{2+}-containing species should not interact with their environment. The low BE also observed for Al^{3+}, K^+ and Mg^{2+} suggests that only a small interaction with their surroundings is possible. As a result, the thin oxide/hydroxide layers were unable to protect the nickel particles from bulk oxidation by air. The high amounts of Ni^{2+} in the form of oxides observed can be a result of exposure to air in the plastic flasks used for storage after the BRM reaction and

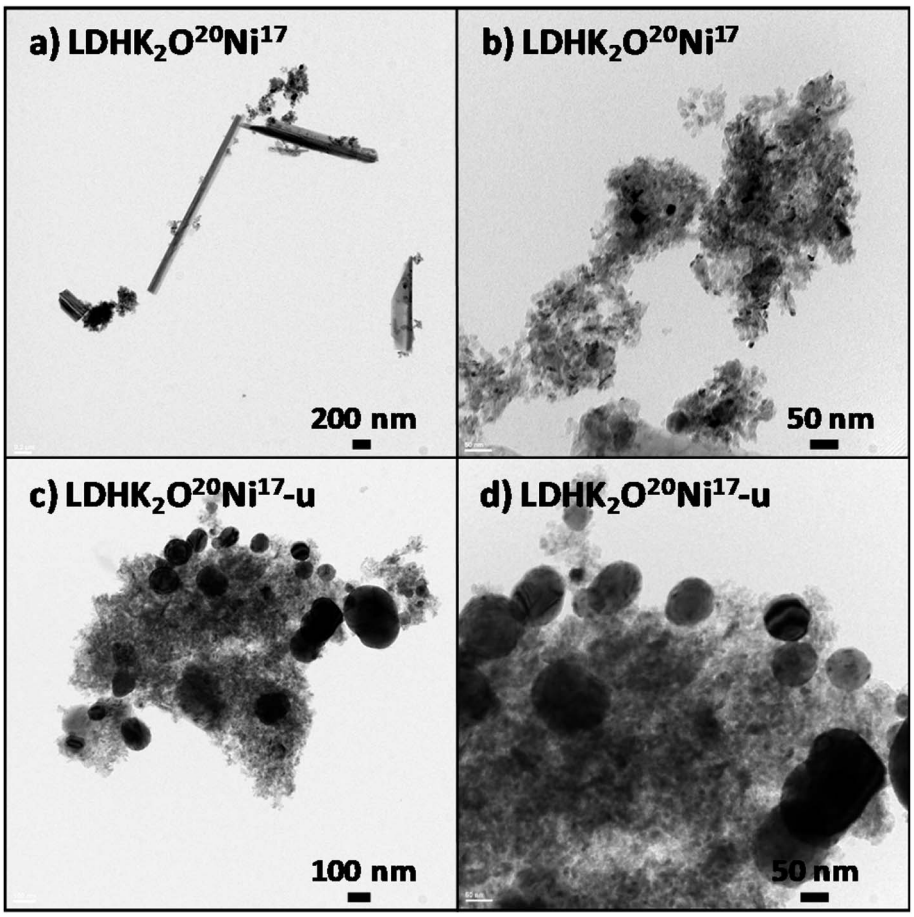

Fig. 4 HAADF-STEM images of the catalysts before (a and b) and after the BRM tests (c and d). (Images have different scales due to the best possible perspective and amplification obtained on the microscope.)

material collection. The XPS spectra of the samples were taken after 24 months of experimental runs. The reason for this procedure is to obtain information about the stability of their oxidation state since it is known that only Ni^0 is catalytically active. However, the high amount of Ni^{2+} on the surface catalytically represents a loss of active sites, which can improve for example the activation of carbon dioxide during BRM. This decrease of Ni on the surface can be seen in Table 3 (from 6 at% to ~4 at%).

The chemical composition of the samples after use in BRM presented changes, *i.e.*, their O content decreased, while their C content increased. All the results should be related with the

Table 4 Comparison of the results in this work and that reported in the literature[12,13,15,16] for BRM

Reference	Catalyst	m_{cat} (g)	Ni (wt%)	T (°C)	p_{total} (kPa)	$\dot{V}_{total}$ (N cm^3 min^{-1})	$\dot{V}_{CO_2}$ (N cm^3 min^{-1})	$X_{CO_2}^{eq}$ (%)	$X_{CO_2}^{average}$ (%)
10	$NiAl_2O_3$	15	15	800	101.3	110	10	91.9	26.4
				700				77.6	18.5
				600				48.6	11.2
12	$NiZrO_2$	0.05	8	800	101.3	40	13	87	82
				650				57	50
13	NiMgO	0.4	4	900	101.3	417	96	n.a.	55
				750				n.a.	33
15	$NiAl_2O_3$	0.05	10	800	101.3	2300	644	92	80
				600				0	0
16	$NiLa_2Zr_2O_7$	0.05	1	800	101.3	1645	164.5	92	52.1
				700				84	41.9
(This work)	$LDHK_2O^{20}Ni^{17}$-u	15	16.7	800	101.3	110	10	91.9	64.6
				700				77.6	42.5
				600				48.6	3.4

different catalytic activities of the samples in the BRM, and the formation or deposition of carbon during the BRM.

In Table 4 it can also be seen that the surface content of Al, K and Mg did not decrease significantly after the reaction, while for Ni the decrease corresponds to about 1/3 or 33%. Indeed, this is a clear explanation for the good catalytic performance of the $LDHK_2O^{20}Ni^{17}$-u material during the BRM since it is known that Al_2O_3 is a textural promoter,[52] as well as MgO in the context of CMD.[53] The effect of Al_2O_3 (also K_2O and MgO) on the surface can also be interpreted as an ensemble size control, *i.e.* the number of adjacent active sites obtained by dilution with Al_2O_3 instead of using a metal such as copper.[54] However, the increase in carbon on the surface is a sign of some deactivation since encapsulating carbon is formed,[55] thus hindering access to the active nickel sites on the catalyst.

3.2 Catalytic performance

The conversion of methane, carbon dioxide and water and the product distribution at the outlet of the reaction unit over the selected materials, LDH, $LDHK_2O^{20}$ and $LDHK_2O^{20}Ni^{17}$, are shown in Fig. 5, 6 and 7, respectively. In addition, the thermodynamic equilibrium conversions of the reactants fed as a function of reaction temperature, and the composition of the product distribution are also included in these figures. The equilibrium calculations were performed using the free available software KOMPLEX (http://physchem.hs-merseburg.de) developed by Martin-Luther-Universität Halle-Wittenberg, Zentrum für Ingenieurwissenschaften (Prof. Dr Dieter A. Lempe), and Hochschule Merseburg (FH), University of Applied Sciences, FB Ingenieur- und Naturwissenschaften (Prof. Dr Gerd Hradetzky).[56] X_i (%) is the conversion of species, while X_{eq} (%) is the equilibrium conversion depicted as dashed lines.

This was done for comparison purposes and to evaluate the catalytic performance. A thermodynamic analysis was already performed in a previous review[9] (Fig. S3, ESI†). Both models show similar results in terms of methane conversion and the same qualitative behavior. However, in the case of carbon dioxide, the obtained results were significantly different since several side reactions are considered in the prediction model used.

In the temperature range of 700 °C to 1100 °C (Fig. S3a,† thermodynamic conversion), the conversion of carbon dioxide was much lower than that of methane, and as the temperature increased, the equilibrium conversion of methane and carbon dioxide tended to the same values (*e.g.* $T_{reaction} = 700\ ^\circ C \rightarrow X^{eq}_{CO_2} \cong 40\%$, $X^{eq}_{CH_4} \cong 80\%$; $T_{reaction} = 800\ ^\circ C \rightarrow X^{eq}_{CO_2} \cong 80\%$, $X^{eq}_{CH_4} \cong 90\%$). Besides, an increase in pressure led to a decrease in carbon dioxide conversion by DRM, while the WGS reaction was favored, a situation that was visible for higher hydrogen-to-carbon monoxide ratios ($H_2 : CO_2 = \sim 6 \rightarrow T_{reaction} = 700\ ^\circ C$ and $p_{reaction} = 1.0$ MPa and $H_2 : CO_2 = \sim 2.5 \rightarrow T_{reaction} = 800\ ^\circ C$ and $p_{reaction} = 0.1$ MPa). The results show that carbon dioxide is the key reactant that controls the reaction system performance. It was also found that the hydrogen-to-carbon ratio obtained decreased to a value close to two, with an increase in reaction temperature, a situation desirable to efficiently obtain methanol from the BRM reaction products.

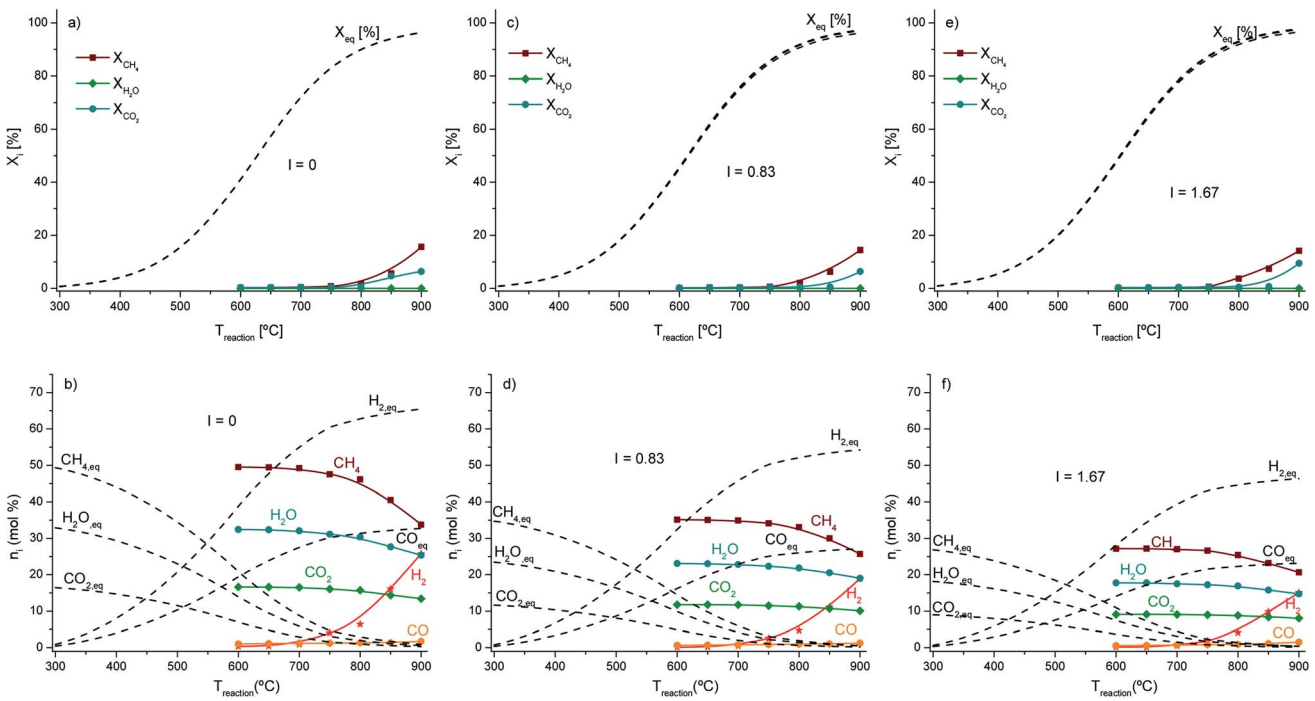

Fig. 5 BRM on LDH. Methane (square symbols), carbon dioxide (rhombus symbols) and water (spherical symbols) conversions (a), (c) and (e), and product distribution (b), (d) and (f) as a function of reaction temperature at steady-state conditions, respectively. Operating conditions: $m_{cat} = 50.0$ g; $p_{total} = 101.3$ kPa; $\dot{n}_{inert} = 0$ (or $\dot{V}_{inert} = 0$ N cm^3 min^{-1}) for (a and b), $\dot{n}_{inert} = 1.028$ (or $\dot{V}_{inert} = 25$ N cm^3 min^{-1}) for (c and d) and $\dot{n}_{inert} = 2.055$ (or $\dot{V}_{inert} = 50$ N cm^3 min^{-1}) for (e and f).

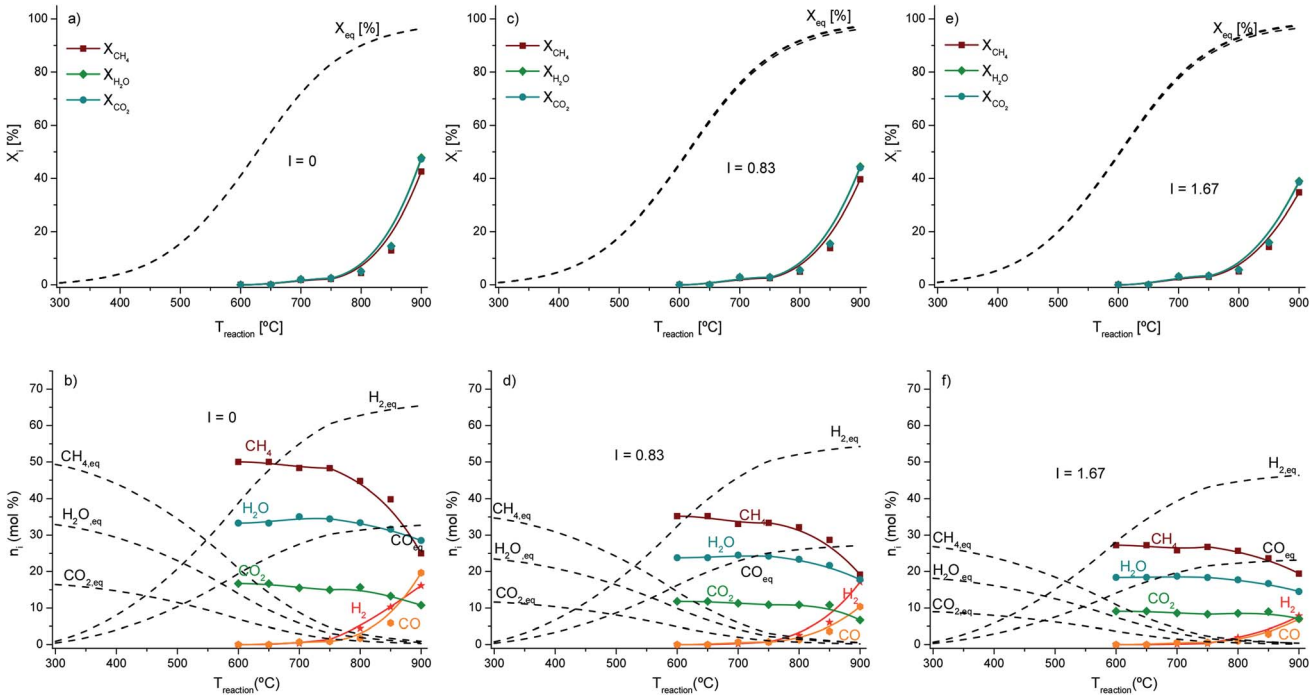

Fig. 6 BRM on $LDHK_2O^{20}$. Methane (square symbols), carbon dioxide (rhombus symbols) and water (spherical symbols) conversions (a), (c) and (e), and product distribution (b), (d) and (f) as function of reaction temperature at steady-state conditions, respectively. Operating conditions: m_{cat} = 50.0 g; p_{total} = 101.3 kPa; $\dot{n}_{inert}$ = 0 (or $\dot{V}_{inert}$ = 0 N cm^3 min^{-1}) for (a and b), $\dot{n}_{inert}$ = 1.028 (or $\dot{V}_{inert}$ = 25 N cm^3 min^{-1}) for (c and d) and $\dot{n}_{inert}$ = 2.055 (or $\dot{V}_{inert}$ = 50 N cm^3 min^{-1}) for (e and f).

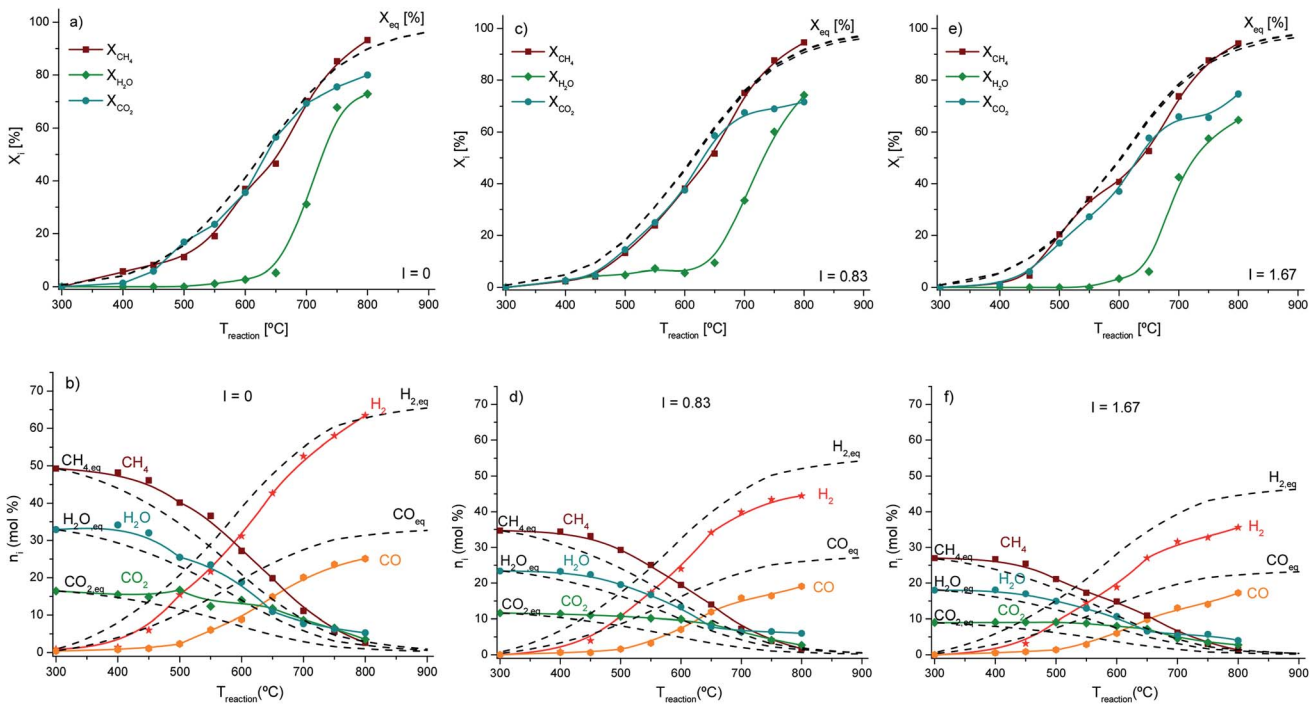

Fig. 7 BRM on $LDHK_2O^{20}Ni^{17}$-u. Methane (square symbols), carbon dioxide (rhombus symbols) and water (spherical symbols) conversions (a), (c) and (e), and product distribution (b), (d) and (f) as a function of reaction temperature at steady-state conditions. Operating conditions: m_{cat} = 15.0 g; p_{total} = 101.3 kPa; $\dot{n}_{inert}$ = 0 (or $\dot{V}_{inert}$ = 0 N cm^3 min^{-1}) for (a and b), $\dot{n}_{inert}$ = 1.028 (or $\dot{V}_{inert}$ = 25 N cm^3 min^{-1}) for (c and d) and $\dot{n}_{inert}$ = 2.055 (or $\dot{V}_{inert}$ = 50 N cm^3 min^{-1}) for (e and f).

Before starting the evaluation of the performance of the catalytic materials used, it must be stressed that thermodynamic calculations clearly indicate that the BRM requires very high reaction temperatures for the reasonable conversion of reactants into an adequate syngas composition. For instance, a conversion of ~80% of all reactants used will theoretically require a reaction temperature of 750 °C. Furthermore, dilution with inert gas affects the reaction as it leads to higher conversion of the reactants.

As expected, the methane, carbon dioxide and water conversion increased with temperature, as shown in Fig. 5–7, respectively. However, the product distribution is not in agreement with the expected stoichiometry of the BRM reaction, indicating that side reactions occurred, especially carbon deposition.[9] The thermodynamic equilibrium conversions and product distributions as a function of reaction temperature calculated with the abovementioned software are also included in the same figures for comparison.

The three main side-reactions that lead to carbon formation are hydrocarbon cracking/catalytic methane decomposition (CMD), Reaction (e);[57] carbon monoxide disproportionation or Boudouard reaction (BD), Reaction (f);[58] and carbon monoxide reduction or reverse coal gasification (RCG), Reaction (g).

$$CH_4 \rightleftharpoons C + 2H_2,\ \Delta_r G^\circ = (-74.9\ \text{kJ mol}^{-1} - T\,(\text{K}) \times -80.6\ \text{J mol}^{-1}\ \text{K}^{-1}) \quad \text{(e)}$$

$$2CO \rightleftharpoons C + CO_2,\ \Delta_r G^\circ = (-172.4\ \text{kJ mol}^{-1} - T\,(\text{K}) \times -320.2\ \text{J mol}^{-1}\ \text{K}^{-1}) \quad \text{(f)}$$

$$CO + H_2 \rightleftharpoons C + H_2O,\ \Delta_r G^\circ = (-175.3\ \text{kJ mol}^{-1} - T\,(\text{K}) \times -109.1\ \text{J mol}^{-1}\ \text{K}^{-1}) \quad \text{(g)}$$

CMD starts to be significant at relative low temperatures, ~400 °C, and both the CMD and the BD reactions are prevalent at temperatures lower than 400 °C. However, at these temperatures, the concentrations of carbon monoxide are low, thus only CMD needs to be considered.

Finally, SRM is an endothermic reversible reaction. It can be seen in all the experimental results (Fig. 5–7 in positions a, c and e) that at a lower reaction temperature range (300–600 °C), the SRM reaction was dominant. This is well-seen for the partial pressure of carbon dioxide obtained at the temperature range observed. It did not significantly change and remained close to the feed conditions with almost no carbon dioxide conversion. The dominance of the SRM reaction at this temperature range was also confirmed by analyzing the hydrogen-to-carbon monoxide ratio, which decreased with an increase in temperature. Here, it must also be stressed that the WGS reaction may influence at a certain range of partial pressure of carbon dioxide because it is a reversible exothermic isochoric reaction, which may add some carbon dioxide back to the overall BRM.

It was also found for all the materials used in this work that higher flow rates increased the conversion of the reactants and the yield of syngas. Since BRM is a dynamic equilibrium, we considered the Le Châtelier's principle (principle of the smallest constraint), which indicates a small change in conditions results in disturbance, and thus the equilibrium position shifts to counteract the change so that equilibrium is reestablished. BRM is not only a reversible endothermic reaction, it is also an exochoric ($\Delta_r V > 0$) volume increase reaction, which means the introduction of inert gas in a system of constant pressure results in a shifting of the equilibrium to the direction with a greater number of mol in gas (so-called dilution effect on the left side of the equilibrium, which is dynamically adjusted to counteract the original number of mol or concentration). The higher the amount of inert gas used, the higher the conversion of the respective reactant. Apparently, this seems to be a contradiction because a higher flow rate means a lower contact time, and therefore lower conversion of the reactants. However, all the catalysts used in this work only sped up the reaction velocity, and did not interfere in the direction of the equilibrium. Since thermodynamics postulates only the maximum reachable achievement, kinetics describes the timescale of change and the underlying mechanism. Besides, one can speculate about mass transfer resistances due to the clusters (active metal, promoters used or even cluster of the support material) located on top of each porous support material used, which can affect the external diffusion by limiting it so that lower catalytic activities for lower flow rates would be obtained. The SEM micrographs support this conclusion, but indeed the catalysts used are not of particularly high surface area, and by increasing the temperature they operated close to equilibrium. The most obvious explanation is the fact that BRM is an endothermic and volume increase reaction, meaning that the conversion of all the reactants involved an increase in temperature with higher inert gas flow rates, as thermodynamically proven in a previous study.[59] Considering the side reaction scheme proposed in our previous works,[9,10] in particular CMD, SRM and DRM, the results obtained from the thermodynamic equilibrium calculations for inert gas variations are effectively clear. The exception is the single WGS reaction equilibrium, also a possible side-reaction, is not affected by the total pressure or partial pressure of inert gas.[59]

The material selected as a support for the promoter and active phase, LDH, as shown in Fig. 5, exhibited poor catalytic activity at low temperatures and reasonable catalytic activity at very high temperatures of around 850 °C and higher. The reason for the poor catalytic activity is most probably due to the deficit of unpaired valence electrons, which are not provided by the respective materials for the catalytic activation of the molecules involved. Considering the chemical structures of the LDH material, it can be found that it belongs to the class of hydrotalcites with a brucite-like structure.[60,61] Hydrotalcite-like materials are preferentially used as support materials in catalysts due to their alkaline properties[25,62] and ability to adsorb carbon dioxide.[23,63] In the former case, it is expected that the LDH structure is totally destroyed at 600 °C due to the thermal effect,[38] and it is expected that a mixed oxide consisting of MgO and Al_2O_3 would be obtained. Indeed, the results obtained from XRD in Section 3.1.2 of this work clearly show the formation of an $MgAl_2O_4$ phase, which corresponds to a spinel (ICDD 77-1193). This type of material has the general formula AB_2O_4 and is chemically and thermally very stable, which is beneficial for

its application in catalytic reactions.[64,65] The cations present in the spinel probably allow internal redox reactions and oxygen mobility, which is the reason why activity was observed above 600 °C (Fig. 5a, c and e). In the latter case, it is also confirmed that above 600 °C, the adsorption of carbon dioxide is almost nil due to the fact that it is an exergonic process ($\Delta_{ad}G < 0$).

Since it is known from the experimental results that the product distribution is not in agreement with the expected stoichiometry of the BRM reaction, where a hydrogen-to-carbon monoxide ratio of two is desirable, this indicated that side reactions occurred, such as the decomposition of methane into hydrogen and carbon (eqn (e)).[49] This was confirmed by comparing the materials before and after the reaction, in particular the carbon deposits on the catalyst surface evidenced by XPS (results above).

In the next step, potassium as a promoter was introduced in the alkaline material for a possible enhancement in performance. Fig. 6 depicts the experimental results obtained for $LDHK_2O^{20}$. The $LDHK_20^{20}$ material performed better compared with pure LDH, in particular at very high temperatures. This can be explained by the electronic promoter nature of K_2O.[25,66] Since K_2O was dispersed in the LDH, considering it as an active phase, it may be possible that it acted as an electronic promoter-electron donor since the chemical binding of the adsorbates could be influenced to increase the reactant conversion. The electronic promotion of K_2O together with the oxygen mobility of the spinel phase $MgAl_2O_4$ exhibited a synergetic effect, which explains the slightly better performance compared to that of the previous material used. This can be clearly seen by comparing Fig. 5a, c and e with Fig. 6a, c and e, respectively, where the conversions obtained *e.g.* at 900 °C are almost 6 times higher.

It can be also observed that the ratio of hydrogen to carbon monoxide changed since potassium oxide is present in the LDH. In contrast, at 900 °C, the hydrogen-to-carbon monoxide ratio was around two to three, and in the K_2O-promoted LDH the hydrogen-to-carbon monoxide ratio was close to one. Most probably, K_2O also acts as a structure promoter, which means the number of possible reactions for the adsorbed molecules decreases, increasing the selectivity due to a dominating reaction or favored reaction pathway. Thus, it is expected that this promoter is directly involved in the solid-state reaction of the catalytically active LDH surface.

In another catalytic reaction, a potassium-promoted LDH was also used to catalyze the water–gas-shift reaction (WGSR).[28] Since the WGSR reaction has a fast kinetics at the expense of a less favorable chemical equilibrium, the formation of carbon monoxide and water is favored at high reaction temperatures. This is another obvious explanation why almost no carbon dioxide was consumed in the temperature range of 300–600 °C, as can be observed in Fig. 6b, d and f.

The potential of using catalytic BRM to produce synthesis gas for the further production of methanol has been discussed in some reviews.[7,9,67,68] The data collected show that the catalysts for reforming processes used Ni as the active phase since it is well established that it is a good phase to activate carbon–carbon, hydrogen–carbon or hydrogen–hydrogen σ-bonds. In commercial catalysts for steam reforming, alumina is routinely used as a support.[59,69] However, alumina supports normally have acid sites, which cause the deposition of carbon. Due to the alkaline feature of LDH, these materials are also useful in the catalytic SRE process to avoid carbon deposition through the formation of ethylene, which is known as a coke precursor. Therefore, HTlc can be a suitable support material for the active phases in catalysts.

It is also reasonable to assume that the formation of an intermediate complex is crucial for a successful catalytic reaction. Thus, it should be beneficial to use a bifunctional catalytic material that selectively adsorbs water and carbon dioxide and holds them for a certain time, increasing their successful reaction probabilities. Accordingly, Ni dispersed on a selective carbon dioxide sorbent/molecular sieve, such as LDH, is expected to catalyze the reversible BRM under conditions close to thermodynamic equilibrium. This can work even better if promoters are introduced, such as the previously tested K_2O. The results for the synthesized catalytic materials are depicted in Fig. 7, where 17 wt% Ni was dispersed with the previously used and discussed promoter (K_2O) in dispersion amounts of 20 wt% on their respective adsorptive support material, LDH.

The results are also presented with helium as an inert gas in the feed stream. The reasons for its use are as follows: firstly, to demonstrate the potential of the novel catalytic materials for the BRM, and secondly, to simulate amounts equivalent to a dilution closer to what would be used in industrial scale processes, also minimizing costs with purification steps needed to obtain a proper reaction feed from easily available raw materials. A typical example is biogas, which has a volume composition ranging from 0–10 vol% N_2, 25–50 vol% CO_2, 50–75 vol% CH_4 and 0–2 vol% of remaining impurities such as H_2O, H_2S, O_2 and H_2.

The conversions of methane, water and carbon dioxide and the product distribution obtained over $LDHK_2O^{20}Ni^{17}$ are shown in Fig. 7. The conversions of the reactant methane, water, and carbon dioxide increased with temperature, as expected, at an earlier stage (around 400 °C) due to the presence of the transition metal nickel in an "S-shape" form. The S-curve concept is normally used in economics, management, and strategic innovation management in the economy[70] as an instrument do identify if there is room to increase the performance of a given system, for example revenue, by increasing the value of a variable, for example price.

As an analogy, the slope of the "S-shaped" conversion curves can indirectly describe the increase in the activity of the catalyst resulting from an extra increase in energy supply to increase the temperature, as shown in eqn (7) and (8)

$$A = \frac{\mathrm{d}X_i}{\mathrm{d}T} = \frac{X_i^2 - X_i^1}{T_2 - T_1} = \frac{\Delta X_i}{\Delta T} \tag{7}$$

$$I = \dot{Q} = \frac{\delta Q}{\delta t} = \dot{m} \times c_p \times \Delta T + \Delta_v H \times \dot{n} \tag{8}$$

where A is the activity of the catalyst [s^{-1}], X_i is the conversion of species i [—], T is the reaction temperature [K], $\dot{Q}$ is heat flow [J s^{-1}], $\dot{m}$ is mass flow rate [kg s^{-1}], $\dot{n}$ is molar flow rate [mol s^{-1}],

c_p is the heat capacity at constant pressure [J kg^{-1} K^{-1}], and $\Delta_v H$ is the enthalpy of vaporization [J mol^{-1}].

Among the fed reactants, methane showed the highest conversion rates, while carbon dioxide the lowest. Only valid for LDHK$_2$O^{20}Ni^{17} in this work, the carbon dioxide conversions were low at low temperatures and increased strongly with an increase in temperature, reaching a plateau of $dX(CO_2)/dT \sim 0$, behavior that was previously described as an S-shaped-curve. The reason for this is the very high activation energy required for carbon dioxide molecule destabilization. In particular, the bond energy in the O=C=O molecule is 745 kJ mol^{-1}, while for methane or water this energy is almost two times lower, 413 and 463 kJ mol^{-1}, respectively. Therefore, it can be concluded that the steam reforming of methane (SRM: $CH_4 + H_2O \rightarrow CO + 3H_2$) starts at lower temperature states and it is easier than the dry reforming of methane (DRM: $CH_4 + CO_2 \rightarrow 2CO + 2H_2$), which occurs at higher temperatures. It must be noted that BRM is a combination of SRM plus DRM, and the results show that the full reaction only occurs at high temperatures.

These conclusions are also supported by the reaction product distribution. Since the DRM is the most difficult reaction to be performed in terms of energy (temperature) input, while SRM and WGS are easier to be conducted under the same conditions, at lower temperatures, the hydrogen-to-carbon monoxide ratio should be very high. On the other hand, when the reaction temperature is increased, DRM becomes more favorable compared with WGS, which explains the approximation of the hydrogen-to-carbon monoxide ratio to two.

Comparing these results with the previous results obtained in Fig. 5 and 6, it is clear that the introduction of Ni as an active phase significantly increased the catalyst performance. By comparing Fig. 7a, c and e with Fig. 6a, c and e, respectively, one can see that, *e.g.* at 800 °C, the conversions of carbon dioxide were *ca.* 75% *vs. ca.* 5%. The reason for this strong activity differences is due in the presence of Ni. As previously mentioned, this active phase has many unpaired valence electrons ([Ar] $3d^8$, $4s^2$), especially in the excited state, which are suitable to activate C–C, H–H, H–C, H–O, C–O single bonds and C=C and C=O double bonds. Thus, combined with the most possible electronic and structural promoter effects of K_2O, a synergetic effect is obtained. Here, it must be stressed that in the case of LDHK$_2$O^{20}, indeed the active phase is K_2O, but its activity is quite low at high temperatures. In the case of LDHK$_2$O^{20}Ni^{17}, the active phase is of course Ni since the conversions increased significantly at moderate reaction temperatures. Thus, we can fairly assume that the role of K_2O is a promoter, and in a reduced range also a synergy of active phases.

It can also be observed in Fig. 7b, d and f compared with Fig. 6b, d and f, respectively, that the hydrogen-to-carbon ratio significantly changed, *e.g.* at 800 °C, the ratios were around 2.5 for the former cases, while in the latter case the ratios of *ca.* 1.5 were observed. The reason for this is associated with the alkaline features of LDH and K_2O, which avoid side-reactions such as CMD or ethylene that provoke carbon deposition on the catalyst surface and consequent deactivation of the catalyst. This is another synergetic effect since Ni enhances the reforming reactions (SRM and DRM). However, at 600 °C the LDH structure is totally destroyed and a magnesium aluminum oxide ($MgAl_2O_4$) spinel phase is obtained, which may reduce the basic nature of the support to a certain degree due to the possible appearance of oxygen mobility, as previously mentioned. Here, it must be stressed that no carbon deposits were detected (check XRD patterns), which confirms the assumptions made. Nevertheless, some increase in carbon content was observed on the surface of the material used, as evidenced in the XPS analysis (from 10.5 wt% for LDHK$_2$O^{20}Ni^{17} to 18.3 wt% for LDHK$_2$O^{20}Ni^{17}-u), which could be the influence of formed $MgAl_2O_4$ (less basicity). In addition, the SEM and TEM analysis of LDHK$_2$O^{20}Ni^{17}-u also showed that no carbon filaments were formed during the reaction, thus the carbon formed on the surface (XPS results) is most probably encapsulating in nature.[49] According to this finding, the ratio of steam-to-methane (in this work 0.5) or better carbon dioxide-to-methane (in this work 0.33) is recommended to be slightly increased,[46] or slight pressure is used to reduce side-reactions such as CMD, as it was done by the research group of Olah *et al.*[11]

Comparing the obtained results in Fig. 7 with a previous report,[10] it is also clear that LDHK$_2$O^{20}Ni^{17} performs much better than a conventional steam reformer catalyst from Degussa composed of $NiAl_2O_3$. In the former case, the conversion of methane is higher (and slightly above the thermodynamic prediction) than the water conversion, while for the latter case the conversions of methane and water until 700 °C increases below the maximum possible thermodynamic expectations. Even more drastic are the discrepancies for the conversion of carbon dioxide. For the same reaction conditions, much higher conversions were obtained for the LDHK$_2$O^{20}Ni^{17} system than for $NiAl_2O_3$. Of course, this phenomenon can only be explained by the presence of the K-promoter, which combines the influence of different crystal sizes of Ni on both materials. While the former has a crystal size of 42.1 nm (check Table 3), the latter has a small crystal size of 3.3. The catalyst with a smaller crystal size should have had a better performance; however, the electronic promotion of K in LDHK$_2$O^{20}Ni^{17}, as well as the higher Ni loading of elementary Ni^0 explains the results obtained.

The LDHK$_2$O^{20}Ni^{17} material was activated before the BRM with hydrogen; however, XRD reflects the structure of the bulk phase rather than the surface, and an NiO phase was detected, which is related with the relatively high loading of the catalyst, where NiO in the bulk phase was not reduced. A similar behavior was found earlier[44,48] with high metal loadings. Since the Ni^{2+} species is not available in the reduced Ni^0 form on catalyst surface, a significant amount of active sites are lost, which could of course increase the catalyst performance, especially to activate carbon dioxide properly.

Finally, we can now compare the results obtained in the present study with the results reported for BRM on Ni-based catalysts,[10,12,13,15,16] as shown in Table 4. The experimental conditions are listed, together with the equilibrium carbon dioxide conversion and the average conversion measured after time-on-stream. Catalyst activity can be assessed by comparing

$X_{CO_2}^{average}$ with $X_{CO_2}^{eq}$. The results obtained in this work are consistent with the values reported in the literature, although significant differences can be observed between the values reported in the various studies. It is *e.g.* observed that at 800 °C a commercial catalyst used in a previous work only provided a carbon dioxide conversion of *ca.* 30%, while in this work the conversion was 65%. Both catalysts were tested under the same operating conditions and showed similar Ni loadings (~15 wt%). Thus, it can be fairly concluded that the catalyst used in this work performs better, approximating the equilibrium conditions. For further comparison of the performances of the catalysts reported in the literature and collected in Table 4, the conversion of reactant (eqn (1)–(3)) must be plotted *versus* space velocity (SV). The SV is defined in eqn (9).

$$SV = F_0/m_{cat} \quad (9)$$

where F_0 is the initial flow rate of reactant [$m^3\ s^{-1}$] and m_{cat} the mass of catalyst [kg^{-1}].

Among the reported catalysts, it can be concluded that catalysts with a low Ni loading are a good choice since smaller crystal sizes of the active phase are obtained (≥10 nm), ensuring good catalytic activities. However, it also appears that the negative effect of the higher Ni crystal sizes reported in this work, in particular the decrease in catalytic activity, can be compensated by the presence of the K_2O promoter. Furthermore, the crystal sizes collected in Table 3 together with the direct comparison with Table 4 on catalytic performance suggest that the larger crystals from the bulk phase do not interfere in the catalyst performance. Experimental evidence is also given by the HAADF-STEM observations, which corroborate the occurrence of small Ni particles in the catalysts. In Fig. 4, very small particles together with other large particles can be observed, with the latter responsible for the XRD signals. Small particles do not give peaks by XRD, but are detected by TEM, and these small particles are sufficient to provide performances similar to that reported by other authors.

4. Conclusions

The results presented in this work show that a catalyst consisting of nickel as the active phase and the use of K_2O as a promoter, both supported on a material (MgO/LDH) with alkaline features and capable of selectively adsorbing carbon dioxide, is adequate for the production of synthesis gas *via* the BRM reaction.

A catalyst pre-treatment with hydrogen and Boudouard reaction was performed to reduce nickel oxides into nickel, and to detach nickel particles into smaller ones, thus increasing the catalyst activity and stability.

The good performance of the potassium-promoted catalyst can be explained by the electronic promotion of potassium over the active nickel phase, which induced destabilization on the C═O double bonds of carbon dioxide. The Ni catalyst promoted with potassium and supported on LDH performed better than the Ni catalyst without the promoter. Most probably, this is related to the support material used, which resulted in larger Ni crystal sizes and a decrease in the surface content of Ni and Al.

The influence of the operating variables was also analyzed in detail. Higher temperatures increased the activity of the catalyst, while the absence of inert gas in the feed decreased the catalyst activity. The desired syngas ratio of 2 : 1 could also be reached by using elevated temperatures.

Conflicts of interest

There are no conflicts to declare.

Acknowledgements

To FCT – Fundação para a Ciência e a Tecnologia, for funding research grants SFRH/BPD/105623/2015, SFRH/BPD/112003/2015, and IF/01093/2014 and project IF/01093/2014/CP1249/CT0003. This work was also financially supported by the Spanish project ref. RTI 2018-099224-B100 from ERDF/Ministry of Science, innovation and Universities – State Research Agengy. Authors thank also LSRE (Prof. Alírio Rodrigues and Prof. José M. Loureiro) for supporting this research. Financial support: Base Funding – UIDB/00511/2020 of the Laboratory for Process Engineering, Environment, Biotechnology and Energy – LEPABE – funded by national funds through the FCT/MCTES (PIDDAC) and of POCI-01-0145-FEDER-006984 (Associate Laboratory LSRE-LCM), funded by FEDER through COMPETE2020-Programa Operacional Competitividade e Internacionalização (POCI) and by national funds through FCT. SMT and LMPM acknowledge the financial support from University of Granada (Reincorporación Plan Propio) and the Spanish Ministry of Economy and Competitiveness (MINECO) for a Ramon y Cajal research contract (RYC-2016-19347), respectively. Authors thank CONDEA Chemie (now SASOL) for supplying the sorbent PURAL MG30 impregnated with K_2CO_3 (aluminum magnesium hydroxide, 70% Al_2O_3).

References

1 R. C. Allen, *The Industrial Revolution: A Very Short Introduction*, Oxford University Press, 2017.
2 J. K. Casper, *Greenhouse Gases: Worldwide Impacts*, Facts On File, 2010.
3 K. Liu, C. Song and V. Subramani, *Hydrogen and Syngas Production and Purification Technologies*, Wiley, 2009.
4 S. K. Chawl, M. George, F. Patel and S. Patel, *Procedia Eng.*, 2013, **51**, 461–466.
5 A. Iulianelli, S. Liguori, J. Wilcox and A. Basile, *Catal. Rev.*, 2016, **58**, 1–35.
6 G. A. Olah, A. Goeppert and G. K. S. Prakash, *Beyond Oil and Gas: The Methanol Economy*, Wiley, 2011.
7 N. Kumar, M. Shojaee and J. J. Spivey, *Curr. Opin. Chem. Eng.*, 2015, **9**, 8–15.
8 G. A. Olah, A. Goeppert and G. K. S. Prakash, *J. Org. Chem.*, 2009, **74**, 487–498.
9 B. A. V. Santos, J. M. Loureiro, A. M. Ribeiro, A. E. Rodrigues and A. F. Cunha, *Can. J. Chem. Eng.*, 2015, **93**, 510–526.

10 A. F. Cunha, T. M. Mata, N. S. Caetano, A. A. Martins and J. M. Loureiro, Catalytic bi-reforming of methane for carbon dioxide ennoblement, *Energy Reports*, 2020, **6**, 74–79.
11 G. A. Olah, A. Goeppert, M. Czaun and G. K. S. Prakash, *J. Am. Chem. Soc.*, 2013, **135**, 648–650.
12 W. Li, Z. Zhao, F. Ding, X. Guo and G. Wang, *ACS Sustainable Chem. Eng.*, 2015, **3**, 3461–3476.
13 M. M. Danilova, Z. A. Fedorova, V. I. Zaikovskii, A. V. Porsin, V. A. Kirillov and T. A. Krieger, *Appl. Catal., B*, 2014, **147**, 858–863.
14 A. J. Majewski and J. Wood, *Int. J. Hydrogen Energy*, 2014, **39**, 12578–12585.
15 K. Jabbour, P. Massiani, A. Davidson, S. Casale and N. El Hassan, *Appl. Catal., B*, 2017, **201**, 527–542.
16 N. Kumar, A. Roy, Z. Wang, E. M. L'Abbate, D. Haynes, D. Shekhawat and J. J. Spivey, *Appl. Catal., A*, 2016, **517**, 211–216.
17 V. A. Kirillov, Z. A. Fedorova, M. M. Danilova, V. I. Zaikovskii, N. A. Kuzin, V. A. Kuzmin, T. A. Krieger and V. D. Mescheryakov, *Appl. Catal., A*, 2011, **401**, 170–175.
18 M. Sheng, H. Yang, D. R. Cahela and B. J. Tatarchuk, *J. Catal.*, 2011, **281**, 254–262.
19 T. Boger and A. K. Heibel, *Chem. Eng. Sci.*, 2005, **60**, 1823–1835.
20 V. R. Choudhary, B. S. Uphade and A. S. Mamman, *Catal. Lett.*, 1995, **32**, 387–390.
21 H.-S. Roh, K. Y. Koo, J. H. Jeong, Y. T. Seo, D. J. Seo, Y.-S. Seo, W. L. Yoon and S. B. Park, *Catal. Lett.*, 2007, **117**, 85–90.
22 Y. H. Hu and E. Ruckenstein, *Catal. Rev.*, 2002, **44**, 423–453.
23 D. M. D'Alessandro, B. Smit and J. R. Long, *Angew. Chem., Int. Ed.*, 2010, **49**, 6058–6082.
24 J. W. Snoeck, G. F. Froment and M. Fowles, *Ind. Eng. Chem. Res.*, 2002, **41**, 3548–3556.
25 A. F. Cunha, Y.-J. Wu, P. Li, J.-G. Yu and A. E. Rodrigues, *Ind. Eng. Chem. Res.*, 2014, **53**, 3842–3853.
26 I. Rossetti, N. Pernicone and L. Forni, *Appl. Catal., A*, 2001, **208**, 271–278.
27 K. Coenen, F. Gallucci, P. Cobden, E. van Dijk, E. Hensen and M. van Sint Annaland, *Chem. Eng. J.*, 2018, **334**, 2115–2123.
28 E. R. van Selow, P. D. Cobden, H. A. J. van Dijk, S. Walspurger, P. A. Verbraeken and D. Jansen, *Energy Procedia*, 2013, **37**, 180–189.
29 E. L. G. Oliveira, C. A. Grande and A. E. Rodrigues, *Sep. Purif. Technol.*, 2008, **62**, 137–147.
30 M. N. Moreira, A. M. Ribeiro, A. F. Cunha, A. E. Rodrigues, M. Zabilskiy, P. Djinović and A. Pintar, *Appl. Catal., B*, 2016, **189**, 199–209.
31 S. Kim, S. G. Jeon and K. B. Lee, *ACS Appl. Mater. Interfaces*, 2016, **8**, 5763–5767.
32 Y. N. Takehito Nakano, *J. Comput. Methods Sci. Eng.*, 2007, **7**, 443–462.
33 N. Mahata, A. F. Cunha, J. J. M. Órfão and J. L. Figueiredo, *Appl. Catal., A*, 2008, **351**, 204–209.
34 W. Nils, F. H. Arnold, W. Nils, W. Egon and F. Gerd, *Lehrbuch der Anorganischen Chemie*, De Gruyter, Berlin, Boston, 2008.
35 M. J. Bronikowski, P. A. Willis, D. T. Colbert, K. A. Smith and R. E. Smalley, *J. Vac. Sci. Technol., A*, 2001, **19**, 1800–1805.
36 P. Sinha, A. Datar, C. Jeong, X. Deng, Y. G. Chung and L.-C. Lin, *J. Phys. Chem. C*, 2019, **123**, 20195–20209.
37 M. Králik, *Chem. Pap.*, 2014, **68**, 1625–1638.
38 A. F. Cunha, Y. J. Wu, J. C. Santos and A. E. Rodrigues, *Chem. Eng. Res. Des.*, 2013, **91**, 581–592.
39 Y. J. Wu, P. Li, J. G. Yu, A. F. Cunha and A. E. Rodrigues, *Chem. Eng. Technol.*, 2013, **36**, 567–574.
40 M. J. Climent, A. Corma, S. Iborra, K. Epping and A. Velty, *J. Catal.*, 2004, **225**, 316–326.
41 G. Fornasari, M. Gazzano, D. Matteuzzi, F. Trifirò and A. Vaccari, *Appl. Clay Sci.*, 1995, **10**, 69–82.
42 D. Tichit, M. H. Lhouty, A. Guida, B. H. Chiche, F. Figueras, A. Auroux, D. Bartalini and E. Garrone, *J. Catal.*, 1995, **151**, 50–59.
43 H. A. Prescott, Z.-J. Li, E. Kemnitz, A. Trunschke, J. Deutsch, H. Lieske and A. Auroux, *J. Catal.*, 2005, **234**, 119–130.
44 A. Al-Ubaid and E. E. Wolf, *Appl. Catal.*, 1988, **40**, 73–85.
45 Y. J. Wu, J. C. Santos, P. Li, J. G. Yu, A. F. Cunha and A. E. Rodrigues, *Can. J. Chem. Eng.*, 2014, **92**, 116–130.
46 A. Adamska, A. Malaika and M. Kozłowski, *Energy Fuels*, 2010, **24**, 3307–3312.
47 D. J. Lim, N. A. Marks and M. R. Rowles, *Carbon*, 2020, **162**, 475–480.
48 Y. J. Wu, P. Li, J. G. Yu, A. F. Cunha and A. E. Rodrigues, *Chem. Eng. J.*, 2013, **231**, 36–48.
49 A. F. Cunha, J. J. M. Órfão and J. L. Figueiredo, *Appl. Catal., A*, 2008, **348**, 103–112.
50 N. D. Charisiou, K. N. Papageridis, L. Tzounis, V. Sebastian, S. J. Hinder, M. A. Baker, M. AlKetbi, K. Polychronopoulou and M. A. Goula, *Int. J. Hydrogen Energy*, 2019, **44**, 256–273.
51 J. F. Moulder and J. Chastain, *Handbook of X-ray Photoelectron Spectroscopy: A Reference Book of Standard Spectra for Identification and Interpretation of XPS Data*, Physical Electronics Division, Perkin-Elmer Corporation, 1992.
52 M. A. Ermakova, D. Y. Ermakov, G. G. Kuvshinov and L. M. Plyasova, *J. Catal.*, 1999, **187**, 77–84.
53 J. L. Pinilla, R. Utrilla, R. K. Karn, I. Suelves, M. J. Lázaro, R. Moliner, A. B. García and J. N. Rouzaud, *Int. J. Hydrogen Energy*, 2011, **36**, 7832–7843.
54 A. F. Cunha, J. J. M. Órfão and J. L. Figueiredo, *Int. J. Hydrogen Energy*, 2009, **34**, 4763–4772.
55 Y.-J. Wu, J. C. Santos, P. Li, J.-G. Yu, A. F. Cunha and A. E. Rodrigues, *Can. J. Chem. Eng.*, 2014, **92**, 116–130.
56 D. A. Lempe and G. Hradetzky, *Komplex Software*, Hochschule Merseburg (FH) & Martin-Luther-Universität Halle-Wittenberg, 2000.
57 J. L. Figueiredo, J. J. M. Órfão and A. F. Cunha, *Int. J. Hydrogen Energy*, 2010, **35**, 9795–9800.
58 J. Kopyscinski, R. Habibi, C. A. Mims and J. M. Hill, *Energy Fuels*, 2013, **27**, 4875–4883.
59 A. F. Cunha, M. N. Moreira, A. Mafalda Ribeiro, A. P. Ferreira, J. M. Loureiro and A. E. Rodrigues, *Energy Technol.*, 2015, **3**, 1205–1216.

60 D. I. Ferrer, *Supported Layered Double Hydroxides as CO_2 Adsorbents for Sorption-enhanced H_2 Production*, Springer International Publishing, 2016.
61 G. Fan, F. Li, D. G. Evans and X. Duan, *Chem. Soc. Rev.*, 2014, **43**, 7040–7066.
62 U. Sikander, S. Sufian and M. A. Salam, *Int. J. Hydrogen Energy*, 2017, **42**, 19851–19868.
63 Z. Yong, V. Mata and A. r. E. Rodrigues, *Sep. Purif. Technol.*, 2002, **26**, 195–205.
64 D. Li, M. Lu, Y. Cai, Y. Cao, Y. Zhan and L. Jiang, *Appl. Clay Sci.*, 2016, **132–133**, 243–250.
65 O. Vozniuk, T. Tabanelli, N. Tanchoux, M. J.-M. Millet, S. Albonetti, F. Di Renzo and F. Cavani, *Catalysts*, 2018, **8**, 332–337.
66 M.-R. Li, Z. Lu and G.-C. Wang, *Catal. Sci. Technol.*, 2017, **7**, 3613–3625.
67 K. Jabbour, N. El Hassan, A. Davidson, S. Casale and P. Massiani, *Catal. Sci. Technol.*, 2016, **6**, 4616–4631.
68 I. Ganesh, *Renewable Sustainable Energy Rev.*, 2016, **59**, 1269–1297.
69 A. F. Cunha, Y. J. Wu, F. A. Díaz Alvarado, J. C. Santos, P. D. Vaidya and A. E. Rodrigues, *Can. J. Chem. Eng.*, 2012, **90**, 1514–1526.
70 K. Alisch, *Gabler-Wirtschafts-Lexikon: A–Be*, Gabler Verlag, 2004.